

See discussions, stats, and author profiles for this publication at: <https://www.researchgate.net/publication/49784109>

Plasmon Line Shaping Using Nanocrosses for High Sensitivity Localized Surface Plasmon Resonance Sensing

ARTICLE *in* NANO LETTERS · FEBRUARY 2011

Impact Factor: 13.59 · DOI: 10.1021/nl102991v · Source: PubMed

CITATIONS

163

READS

315

7 AUTHORS, INCLUDING:



Niels Verellen

University of Leuven

56 PUBLICATIONS 1,072 CITATIONS

SEE PROFILE



Pol Van Dorpe

imec Belgium / KULeuven

132 PUBLICATIONS 3,289 CITATIONS

SEE PROFILE



Chengjun Huang

Chinese Academy of Sciences

17 PUBLICATIONS 334 CITATIONS

SEE PROFILE



Guy A. E. Vandenbosch

University of Leuven

485 PUBLICATIONS 3,066 CITATIONS

SEE PROFILE

Plasmon Line Shaping Using Nanocrosses for High Sensitivity Localized Surface Plasmon Resonance Sensing

Niels Verellen,^{*,†,‡,§} Pol Van Dorpe,[‡] Chengjun Huang,[‡] Kristof Lodewijks,^{‡,§} Guy A. E. Vandenbosch,[§] Liesbet Lagae,^{‡,||} and Victor V. Moshchalkov[†]

[†]INPAC-Institute for Nanoscale Physics and Chemistry, Nanoscale Superconductivity and Magnetism and Pulsed Fields Group, K. U. Leuven, Celestijnenlaan 200 D, B-3001 Leuven, Belgium

[‡]IMEC, Kapeldreef 75, 3001 Leuven, Belgium

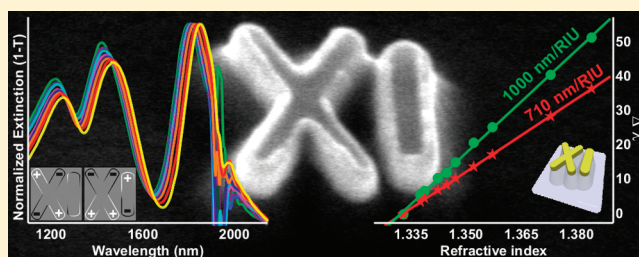
[§]ESAT-TELEMIC, K. U. Leuven, Kasteelpark Arenberg 10, B-3001 Leuven, Belgium

^{||}Physics Department, K. U. Leuven, Celestijnenlaan 200 D, 3001 Leuven, Belgium

S Supporting Information

ABSTRACT: The detection of small changes in the wavelength position of localized surface plasmon resonances in metal nanostructures has been used successfully in applications such as label-free detection of biomarkers. Practical implementations, however, often suffer from the large spectral width of the plasmon resonances induced by large radiative damping in the metal nanocavities. By means of a tailored design and using a reproducible nanofabrication process, high quality planar gold plasmonic nanocavities are fabricated with strongly reduced radiative damping. Moreover, additional substrate etching results in a large enhancement of the sensing volume and a subsequent increase of the sensitivity. Coherent coupling of bright and dark plasmon modes in a nanocross and nanobar is used to generate high quality factor subradiant Fano resonances. Experimental sensitivities for these modes exceeding 1000 nm/RIU with a Figure of Merit reaching 5 are demonstrated in microfluidic ensemble spectroscopy.

KEYWORDS: Fano resonance, LSPR sensing, plasmon hybridization, subradiance, plasmonics, heterodimer



The excitation of collective electron oscillations in metallic nanoparticles (NPs) stands at the origin of the resonant optical extinction from gold and silver NPs—many orders of magnitude higher than the signal from, e.g., fluorophores, fluorescent beads, or quantum dots. Consequently, strong interest from fundamental and application driven research in biomedicine, diagnostics, healthcare, disease treatment, energy, and optical communication has been given to these resonant electron oscillations at the metal–dielectric interface, called *localized surface plasmon resonances* (LSPR).^{1–3}

Recent advances in the synthesis and fabrication of NPs and metamaterials with complex shapes and structures resulted in a growing amount of theoretical and experimental studies on coupled plasmon modes in symmetric and broken-symmetry systems.^{4–11} First of all coupling between individual plasmon modes leads to splitting of the modal energies into bonding and antibonding combinations known as *plasmon hybridization*.⁴ Additionally, reducing the symmetry of the system relaxes the dipole coupling selection rules resulting in an admixture of dipole and higher order modes.^{5,12–14} This coherent mode coupling enables, besides the tunability of the size and shape dependent spectral position of the resonances, the possibility of plasmonic bandwidth and line shape engineering through radiative damping

control.^{15,16} Specifically, the creation of additional sharp spectral features such as subradiant¹⁷ and Fano resonances^{18,19} and plasmonic induced transparency²⁰ presents important potential in applications such as LSPR sensing^{21–25} and plasmonic nano-lasing.^{26,27}

Up to now, refractive index (RI) sensing is by far the most common and successful application area in plasmonics. The sensing principle is based on the plasmon resonance spectral shift caused by a change in the dielectric properties of the environment. LSPRs can detect and allow real-time monitoring of molecular binding events using standard optical transmission spectroscopy (where extinction, the sum of absorption and scattering, is measured) making them valuable bioreporters with superior normal and lateral spatial resolution, ultimately allowing single molecule detection.^{28–30}

In order to reach best sensing performance, the plasmon resonance should have the following basic characteristics: a high spectral shift $\partial\lambda_{\text{LSPR}}/\partial n$ and a narrow line width. In this Letter we show in a series of bulk RI sensing experiments how to boost

Received: August 24, 2010

Revised: November 30, 2010

Published: January 25, 2011

these two requirements in planar Au nanocavity geometries on a glass substrate. The spectral shift per RI unit (RIU) change is proportional to the fraction of the fields and energy density associated with the plasmon excitation located in the sensing medium. We obtain a substantial increase in sensing volume by introducing a selective dry plasma etch of the substrate which can be applied to a vast range of LSPR and lattice based SPR sensors. The increased sensing volume is immediately translated in an important increase in LSPR shift sensitivity as a significant part of the plasmon energy density otherwise trapped in the substrate is now subject to the variable RI of the analytes.³¹ Furthermore, at resonance, the plasmon energy density residing in the dielectric environment depends on the real part of the metal permittivity such that there will be a general increase in the sensitivity for resonances at longer wavelengths.^{32,33} Our resonators were therefore designed to have the plasmon modes at long wavelengths with an upper limit set by strong water absorption bands starting at 1900 nm and the absorption in the polymer of the microfluidic chip used in the sensing experiments. When going beyond the quasi-static limit, radiative losses can increase dramatically with particle size. Getting control over this radiative broadening of the plasmon bands hence is essential to restore high *Q*-factor resonances in the near-infrared (NIR) and requires resonances which forbid strong electric-dipole radiation. We will show both experimentally and in simulations that substantial radiative damping reduction can be obtained by using concepts of Fano interference and subradiance in broken-symmetry nanocavities and that this results in high LSPR sensitivities. In order to make a consistent characterization of these sensitivities of the complex asymmetric modes we also introduce a robust fitting model.

The specific plasmonic nanocavities used in this work are based on a new nanoparticle geometry: the nanocross (Figure 1c). Since the cross geometry has the clear distinct symmetry of a dipole and quadrupole charge distribution, efficient charge separation into these modes is facilitated. These broad dipolar and sharp higher order modes are the necessary ingredients to construct narrow line width subradiant and Fano resonances in a side-by-side arrangement of a nanocross and a nanobar. The cavity structures are schematically shown in Figure 1a with the geometrical parameters indicated: cross length L_c and width W_c , cross arm angle α , bar length L_b and width W_b , cross-bar gap G , Au thickness T , and SiO_2 pillar height H . We will refer to this combination of a cross and a bar as an XI cavity. The sample consists of a standard microscope cover glass with a sputtered 50 nm Au/3.5 nm Ag bilayer. Using electron beam lithography on a negative tone hydrogen silsesquioxane (HSQ) resist coating and subsequent Xe ion milling, the nanostructures are carved out of the metal layers. Although the structural dimensions still require expensive serial lithography steps, advances in nanostencil and nanoimprint lithography suggest that this cost issue can soon be circumvented.^{34,35} In order to partially etch the substrate, an additional sulfur hexafluoride + oxygen ($\text{SF}_6 + \text{O}_2$) plasma etch is performed (Oxford Instruments Plasmalab System 100 ICP 180). This etch is commonly used to target silicon and silicon nitride with volatile fluorides but is also known to etch silicon dioxides.³⁶

Figure 1c–e shows scanning electron microscopy (SEM) images of the sample taken under an angle of 45° after etching. Prior to SEM imaging, a 20 nm thick layer of a conductive polymer is spun on the samples to avoid charging problems. The bright rim on top of the particles results from Au redeposition during the ion-milling. The inset in panel c clearly shows that the

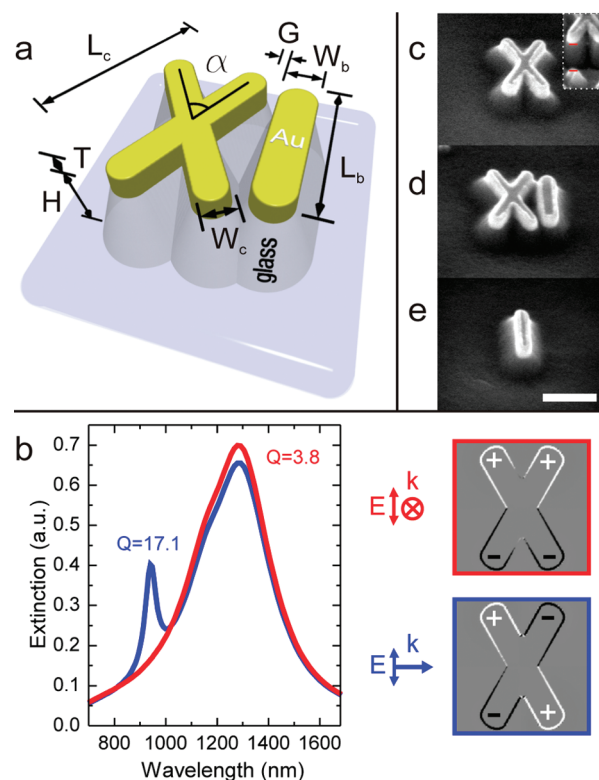


Figure 1. (a) Structural parameters of the studied nanocross cavities. (b) Calculated extinction spectra for a nanocross with $L_c = 380$ nm, $W_c = 76$ nm, $T = 50$ nm, and $\alpha = 60^\circ$ illuminated by a vertically polarized plane wave incident from the top (red line) and from the side (blue line) with calculated charge density distribution of the dipole (top) and quadrupole mode (bottom) and the corresponding *Q*-factors indicated. (c–e) SEM images taken under an angle of 45° of (c) a cross, (d) an XI cavity, and (e) a bar. Scale bar: 200 nm.

Au particles are elevated above the substrate. From these images a height of the SiO_2 support of $H \approx 170$ nm is derived.

The cavities are arranged in $50 \mu\text{m}$ by $50 \mu\text{m}$ arrays with an interparticle distance of $2 \mu\text{m}$ in order to avoid near-field coupling and diffraction related effects. Transmission spectra were taken with a Fourier transform infrared (FTIR) microscope (Bruker Vertex 80v + Hyperion). The incident light from a tungsten lamp is focused on the sample via a $15\times$ magnification, $\text{NA} = 0.4$ reflective Cassegrain condenser and collected in transmission with an identical objective. The transmitted light is then polarized, spatially filtered with a metal knife edge aperture, and detected with a liquid nitrogen cooled mercury–cadmium–telluride (MCT) and Si diode detector. All spectra are normalized to a reference spectrum taken on the bare substrate under identical conditions.

Calculated extinction spectra and surface charge distributions are obtained with a commercial FDTD solver using a mesh of 2 nm .³⁷ For the dielectric permittivity of gold, we used a multi-coefficient model fit to ellipsometry data of the Au films used in our fabrication process. These data match well the values reported in literature.³⁸ The substrate with refractive index $n = 1.45$ was taken into account, except in Figure 1b. The slanted sidewalls of the SiO_2 pillar were not taken into account. All the charge plots are calculated at the middle cross section of the Au structures.

Typical extinction spectra of a nanocross obtained from FDTD simulations are shown in Figure 1b. The red line

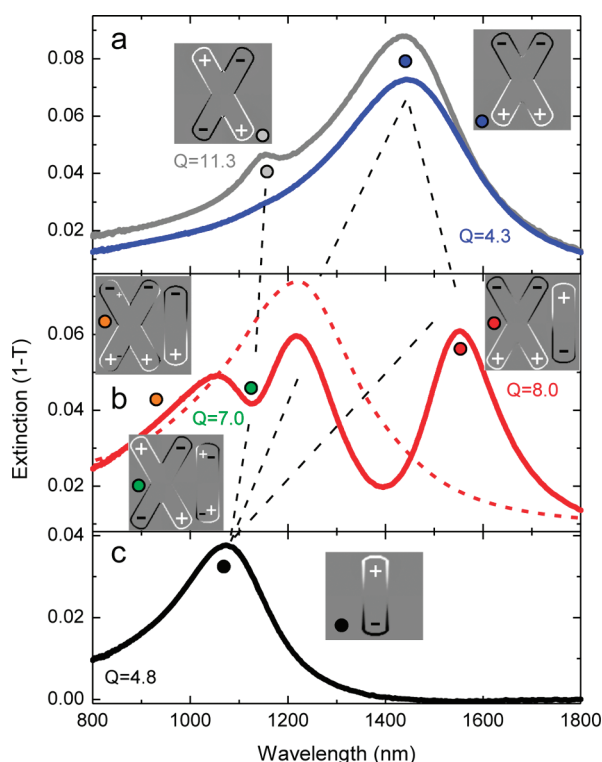


Figure 2. Experimental extinction spectra for vertical polarization: (a) gold cross ($L_c = 380$ nm, $W_c = 76$ nm, $\alpha = 60^\circ$, $T = 50$ nm, $H = 170$ nm) illuminated from the top (blue) and from the side (gray); (b) coupled XI cavity ($L_c = 380$ nm, $W_c = 76$ nm, $\alpha = 60^\circ$, $L_b = 296$ nm, $W_b = 86$ nm, $T = 50$ nm, $H = 170$ nm, $G = 20$ nm) top illuminated (red), subradiant BDD and BQD Fano antiresonance at 1550 and 1125 nm, respectively. The red dashed line indicates the superradiant envelope; (c) gold bar ($L_b = 276$ nm, $W_b = 76$ nm, $T = 50$ nm, $H = 170$ nm) top illuminated (black). Insets: simulated charge distributions associated with the indicated resonances. Corresponding Q -factors are indicated.

corresponds to the nonretarded case where the particle is illuminated from the top and only a broad dipole resonance is excited around 1250 nm (cross dipole mode, D_X). When illuminating from the side at grazing incidence (blue line), we introduce a field gradient along the structure which allows the incident radiation to couple to higher order modes which are dark for normal incidence. And indeed, an additional resonance appears in the spectrum around 950 nm. The charge density plots in Figure 1b clearly illustrate the dipolar (red box) and quadrupolar (blue box) nature of the modes. Since the dark quadrupole mode (cross quadrupole mode, Q_X) couples only weakly to dipolar radiation, it is characterized by a very narrow line width with a full width at half-maximum (fwhm) of 55 nm compared to 350 nm for the dipole resonance. The spectral position of the modes can be tuned first of all with the arm length L_c . Additionally, the spectral position and, more interestingly, the spectral separation of the plasmon modes can be tuned and optimized for specific applications by changing the cross arm angle α . More details about this will be presented elsewhere and we consider here only a cross with $\alpha = 60^\circ$. Figure 2a shows the experimental results corresponding to Figure 1b. The blue curve is obtained at normal incidence. In the gray curve, with illumination at an angle of 70° from the sample normal, the additional peak of the Q_X mode is clearly distinguished. The fwhm's of the D_X and Q_X mode are 300 and 105 nm, respectively. Note that the measured

quadrupole mode is not as intense and sharp as in the calculation. This is a common observation in this type of plasmonic system and can be attributed to extra losses in the metal due to grain boundaries and increased surface scattering.^{39,40} In our case, the absence of the substrate in the calculation and the specific excitation with the Cassegrain objective and smaller angle of incidence resulting in a lower excitation efficiency in the experiment will add to the observed discrepancies (in spectral width and position of the resonances). The experimental extinction spectrum of a Au bar is shown in Figure 2c and features a broad dipole resonance (bar dipole mode, D_1) around 1080 nm with a relatively large fwhm of 220 nm.

Figure 1d shows an SEM image of a coupled XI heterodimer cavity and Figure 2b the experimental top illuminated, vertically polarized extinction spectrum. When the cross and the bar are brought into close proximity, their plasmon resonances couple into three hybridized modes (illustrated with the black dashed lines in Figure 2). The nature of these modes can be deduced from their charge density distributions shown in the insets. The first two modes are a higher energy *antibonding dipole–dipole* combination (ADD) where the cross and bar dipole moments oscillate in-phase (orange dot) and a lower energy *bonding dipole–dipole* mode (BDD) where they oscillate out-of-phase (red dot). Consequently, the ADD mode will have an increased effective dipole moment resulting in a broad *superradiant* envelope (red dashed line) centered around 1230 nm with high radiative losses. While for the BDD resonance at 1550 nm, a reduction of the effective dipole moment results in a strong *subradiant* line width narrowing. Since the narrow BDD mode spectrally overlaps with the tail of the broad superradiant envelope, the requirements for Fano interference are satisfied.¹⁹ As a result the subradiant BDD extinction peak has a typical asymmetric Fano line shape. Down or up scaling of the particle size results in an evolution toward a symmetric subradiant resonance or Fano antiresonance dip, respectively. Although influenced by Fano interference, for the specific XI dimensions chosen in this work, the BDD mode retains its subradiant character and line shape from the electrostatic limit (Figures S1 and S2, Supporting Information). Further on we therefore refer to this extinction resonance as the subradiant BDD mode. The reduced structural symmetry in the XI heterodimer and strong near-field coupling due to the small interparticle separation enable the bar D_1 mode to couple easily to higher order modes in the cross, and vice versa, rendering these modes dipole active. This results in the third hybridized mode: a bonding combination of the Q_X and D_1 mode (*bonding quadrupole–dipole*, BQD). The strong spectral overlap of the narrower BQD and broad ADD mode and their specific relative phases give rise to a destructive Fano interference suppressing the bar dipole moment and hence also radiative losses (scattering). It therefore appears as a narrow antiresonant dip in the extinction spectrum (green dot Figure 2b) roughly at the Q_X resonance with a line width determined by this mode.^{9,12,17,18,41} Note that, as a consequence of the reduced dipole moment in the bar, the higher order mode mixing between cross and bar becomes apparent in the charge plot. Also for the ADD mode (orange dot), where the main mode in the cross is nevertheless dipolar, mode mixing introduces weak higher order components in the charge distribution. This effect is commonly observed in heterodimer systems.^{9,18} A more in-depth analysis of the XI LSPR modes is found in the Supporting Information. Both the subradiant BDD and BQD Fano resonances are sharp spectral features with a strongly reduced line

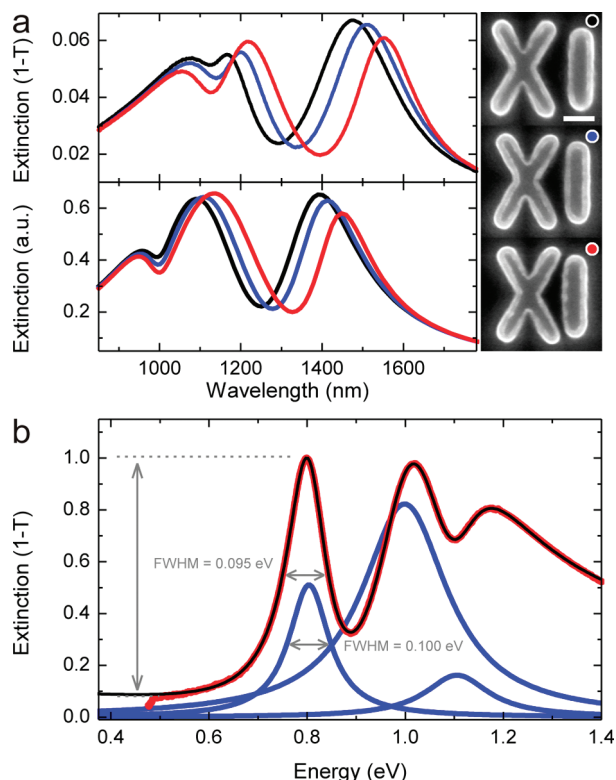


Figure 3. Gap dependence and Fano fitting. (a) Top: experimental extinction spectra for XI cavities with decreasing cross-bar spacing G : black, $G \approx 40$ nm; blue, $G \approx 30$ nm; red, $G \approx 20$ nm (same as Figure 2b). (a) Bottom, simulated extinction spectra corresponding to (a) top with the dimensions taken from the XI structure in Figure 2b. Insets: SEM images of the corresponding fabricated cavities (scale bar, 100 nm); (b) red line, experimental data; black line, three oscillator Fano fit; blue lines, the three oscillators used in the fit.

width compared to the dipole modes of the constituting cross and bar and even enable multiwavelength spectroscopic sensing. Alternatively, heterodimers consisting of two crosses with different size or arm angle will present similar spectral features.

To elucidate the near-field nature of the mode coupling, samples with different gap size G were fabricated. Figure 3a shows experimental (top) and simulated (bottom) extinction spectra for XI cavities with decreasing gap size $G \approx 40$ nm (black curve), 30 nm (blue curve), and 20 nm (red curve). By bringing the particles closer, first of all a stronger hybridization of the dipole modes results in a red shift of the superradiant ADD and subradiant BDD mode.^{4,41,42} More interestingly, the subradiant mode gradually collapses as the out-of-phase oscillating cross and bar dipole moments cancel more efficiently, while the ADD mode broadens. Furthermore, we see that the stronger near field interaction at smaller gap sizes leads to a more pronounced BQD Fano dip due to a more efficient excitation of the Q_X mode.¹⁸

In order to consistently quantify the line widths of the asymmetric Fano resonances, a proper fitting function to the whole spectrum is required. Recently, it has been shown that the amplitude of transmission or reflection from plasmonic lattices as well as the absolute value of the polarizability of disk, ring and disk-in-ring particles can be well described by a Fano-type line shape.^{12,22,43} Here, we demonstrate that far field extinction spectra $E(\omega) = 1 - T(\omega) = |e(\omega)|^2$ of the nanocross

Table 1. Line Width and Q-Factor for the Nanobar and Nanocross in Figure 2 and for the Subradiant BDD and BQD Fano Resonances of the XI Cavities in Figure 3a (top part experimental data, bottom part simulated data)

			line width		
	resonance type	gap G, nm	nm	eV	Q factor
measurement	D _I		220	0.240	4.8
	D _X		330	0.198	4.3
	Q _X		105	0.096	11.3
	BDD _{XI}	40	265	0.152	5.5
		30	240	0.131	6.2
		20	195	0.100	8.0
	BQD _{XI}	40	130	0.128	8.6
		30	170	0.165	6.6
		20	160	0.157	7.0
simulation	BDD _{XI}	40	235	0.150	5.9
		30	210	0.130	6.8
		20	170	0.101	8.5
	BQD _{XI}	40	85	0.110	11.4
		30	90	0.115	10.9
		20	95	0.120	10.3

cavities can also be expressed with an analytical Fano interference model

$$e(\omega) = a_r + \sum_j \frac{b_j \Gamma_j e^{i\phi_j}}{\omega - \omega_j + i(\gamma_j + \Gamma_j)} \quad (1)$$

Here a_n is a constant background amplitude. b_j , ψ_j , and ω_j characterize respectively the amplitude, phase, and resonant energy of the j different oscillators representing the interfering hybridized LSPR resonances. The oscillator line width contains nonradiative damping γ_j due to absorption in the metal and radiative damping Γ_j contributions. It is found that γ_j is negligible as is expected for particles with size $\sim \lambda$.⁴⁴ A nearly perfect match with a three oscillator ($j = 1, 2, 3$) model fit was obtained for all measured and simulated spectra in Figure 3a. An excellent one or two oscillator fit for the cross and bar spectra was found as well. As an example, the black line in Figure 3b shows the fit to the experimental XI spectrum shown in Figures 2b and 3a (red curves). The blue lines represent the three fit oscillators. From low to higher energy we have the oscillator representing the BDD, ADD, and BQD mode, respectively. The corresponding oscillator line widths Γ_{BDD} and Γ_{BQD} will be used further in this work to define the fwhm of the extinction resonances. For the subradiant BDD mode, it is easily seen in Figure 3b that this indeed corresponds to the line width one obtains from the full fit when taking the bottom gray dashed line as baseline. To be more precise, our resulting line width of 0.100 eV (195 nm) is in this way even slightly overestimated compared to the real fwhm of 0.095 eV. For the dip of the BQD Fano mode, it is less obvious how these two values are related. Using a simple Lorentz fit gives similar results; however the exact line width was found to depend sensitively on the spectral window used for the fitting. An alternative method proposed by Hao et al. defines the full width of the Fano resonance as the energy difference between the antiresonance dip and adjacent peak.⁴¹ This results in an even smaller full width of 0.083 eV taking the lower energy peak and 0.076 eV for the higher energy one compared to 0.157 eV from

the fit. Also here it is not immediately clear how this value is related to the line width of the spectral dip at the Fano resonance.

Table 1 gives an overview of the experimental and simulated line widths and Q -factors obtained from our full spectrum Fano fit for the XI cavities in Figure 3a as well as for the bar and cross in Figure 2. An extended table can be found in the Supporting Information (Table S I). For instance, the Q -factors for the $G = 20$ nm XI cavity are $Q_{\text{BDD}} = 8.0$ and $Q_{\text{BQD}} = 7.0$. For the corresponding separate cross and bar the dipole mode Q -factors are only 4.3 and 4.8, respectively, and for the cross quadrupole $Q = 11.3$. Simulations result in $Q_{\text{BDD}} = 8.5$ and $Q_{\text{BQD}} = 10.3$, which are in good agreement with the experimental values. Increasing radiative broadening for red-shifting resonances can thus easily be overcome by proper coupling of bright and dark plasmon modes into subradiant and Fano resonances. Nearly a doubling of the Q -factor can be realized. The effect of reducing the interparticle spacing G on the radiative line broadening of the subradiant BDD mode is striking. An experimental Q -factor increase of 45% and line width reduction of 35% are obtained for a 20 nm gap decrease. Additional narrowing of the gap will push this even further. The same trend is present in the calculations. The influence on the line width of the BQD Fano dip is less dramatic. Although the interference becomes more prominent when the coupling is stronger (see Figure 3a), the resulting line width is set by the width of the Q_x mode and hence does not change significantly. This is clearly seen in the simulations in the bottom panel of Figure 3a. In the measurements, however, small geometrical differences from array to array cause first of all the spectral position of the dip to shift slightly (see, e.g., black and blue curve in Figure 3a top panel) and secondly result in changes in the line shape.

In a series of LSPR sensing measurements a detailed comparison of the bulk LSPR RI sensitivities of the different plasmon modes described above was conducted. A microfluidic chip⁴⁵ was used to supply different glycerol solutions with different RI to the plasmon resonators while extinction spectra were recorded. Figure 4 summarizes the experimental results for the 20 nm gap XI cavity array. Panel a displays the full extinction spectra normalized to the subradiant BDD mode. The noise at 1900 nm is a result of strong spectral absorption in water. To clearly see the spectral shift with increasing refractive index, panel b shows a zoom-in of the normalized BDD mode (bottom curves) and normalized BQD Fano mode (top curves). Even for very small refractive index changes, a clear spectral shift can be resolved for both modes. For instance, the difference in refractive index from the red (4% glycerol concentration) to the blue (5%) spectrum is only 0.0012. The spectral shift $\Delta\lambda_{\text{res}}$ relative to water ($n = 1.333$) versus refractive index of the surrounding liquid is plotted in panel c. A linear fit to the data gives a big RI sensitivity $\delta\lambda/\delta n$ of 1000 nm/RIU for the BDD mode (blue) and 710 nm/RIU for the BQD Fano resonance. Additionally, the RI sensitivity should be quantified by taken into account the fwhm of the resonances. This results in the so-called figure of merit: $\text{FoM} = (\delta\lambda/\delta n)/\text{fwhm} [(\text{eV}/\text{RIU})/(\text{eV})]$.⁴⁶ To get a consistent estimate for this value, we use the line widths obtained from a full Fano model fit and as such obtain a FoM of 4.6 for the subradiant BDD and 4.1 for the BQD Fano mode. Taking the line width proposed by Hao et al., we arrive at a FoM of 12.5 for the BQD Fano mode (see Table S II in the Supporting Information). To the best of our knowledge these are the highest LSPR sensitivities obtained in ensemble measurements reported to date.^{1,3} In a recent extensive study Chen et al. reported FoM values ranging

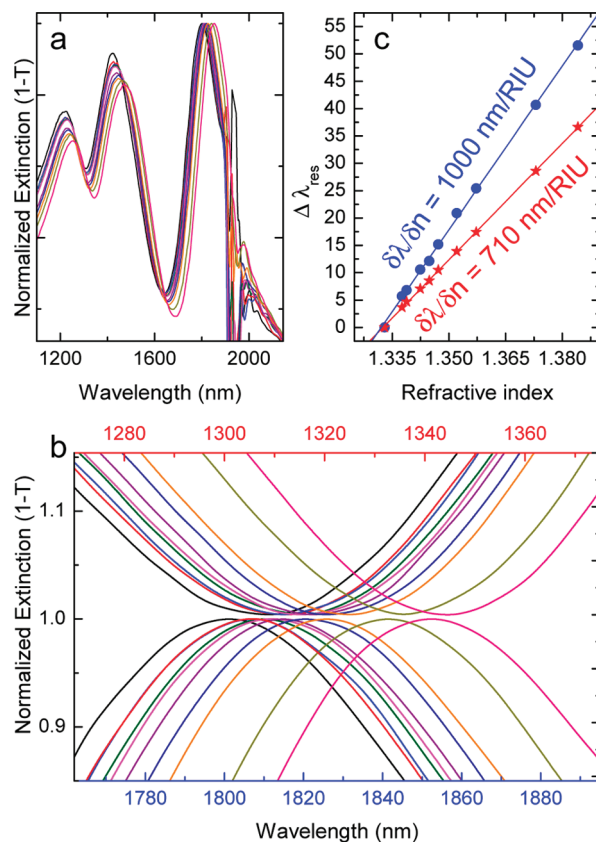


Figure 4. RI sensing results for the XI cavity in Figure 2b. (a) Complete spectra for 0 (black), 4 (red), 5 (blue), 8 (green), 10 (magenta), 12 (purple), 16 (navy), 20 (orange), 32 (dark yellow), and 40% (pink) glycerol solutions normalized to the subradiant BDD mode (spectral resolution 32 cm^{-1}). (b) Zoom-in on the BDD (bottom part) and BQD Fano resonance (top part) showing the spectral shifts in more detail. (c) Spectral shift $\Delta\lambda_{\text{res}}$ relative to water ($n = 1.333$) vs RI of the surrounding liquid. Dots are the experimental data points, lines are linear fits to the data giving a RI sensitivity of 1000 nm/RIU and 710 nm/RIU for the subradiant BDD (blue) and BQD Fano resonance (red), respectively.

from 0.6 for Au nanospheres to 4.5 for nanobipyramids.⁴⁷ A refractive index sensitivity of 588 nm/RIU and FoM of 3.8 were recently demonstrated for an electromagnetically induced transparency (EIT) based planar metamaterial.²⁴ Higher FoM numbers up to 5.7 were obtained only in single particle measurements on chemically synthesized Au stars⁴⁸ and Ag cubes⁴⁶ and plasmonic nanoclusters.²⁵ In the simulations we obtain slightly better results (see Table 2: $\text{FoM}_{\text{BDD}} = 5$ and $\text{FoM}_{\text{BQD}} = 5.5$).

To reveal the origin of the high sensitivities, we make a comparison of the XI cavities with different G and the D_I and D_X modes. Since generally $(\delta\lambda/\delta n)$ is higher at longer λ_{res} , L_b and L_c were chosen such that the resonance positions are comparable with the BDD and BQD modes in the XI cavities. The experimental results are summarized in Table 2. Although small differences up to 5% are observed in the spectral shift/RIU between the longer bar, cross, and BDD_{XI} mode, no significant shape or plasmon mode dependence can be concluded. The same is true when we compare the D_I resonance of the smaller bar with the BQD Fano resonance. These findings are in accordance with theoretical considerations in the quasi-static limit where bulk RI sensitivities are found to only depend on the resonant wavelength and the dielectric properties of the metal

Table 2. Summary of RI Sensitivities (spectral shift (shift/RIU) and FoM) for Different Structures: a Bar (I) with $L_b = 280$ and 430 nm and $W_b = 76$ nm, a Cross (X) with $L_c = 380$ nm and $W_c = 76$ nm, and the XI Cavities from Figure 3^a

	resonance type	L_b, L_c, G , nm	resonance, nm	line width, nm	shift/RIU, nm	FoM
measurement	D _I	L_b 280	1250	280	675	2.4
	D _I	L_b 430	1765	335	1035	3.1
	D _X	L_c 380	1695	345	990	2.9
	BDD _{XI}	G 40	1725	275	1020	3.7
		G 30	1760	250	980	3.9
		G 20	1800	215	1000	4.6
	BQD _{XI}	G 40	1305	145	685	4.7
		G 30	1320	195	705	3.6
		G 20	1305	175	710	4.1
simulation	BDD _{XI}	G 40	1745	320	1140	3.6
		G 30	1765	275	1125	4.0
		G 20	1815	225	1140	5.0
	BQD _{XI}	G 40	1240	130	850	6.6
		G 30	1240	140	805	5.7
		G 20	1240	155	860	5.5

^a Resonance values taken in water ($n = 1.333$) solution, resonant wavelength and line width are also tabulated: top part, experimental data; bottom part, simulated data. An extended table can be found in the Supporting Information (Table S II).

and the medium.^{32,33} Although, strong shape dependent RI sensitivities where the sensitivity is generally found to increase for more elongated particles with sharper apexes have been reported.⁴⁷ In our current study, however, all particle aspect ratios and apex sizes are limited by the resolution in the electron beam lithography and hence are similar. We therefore attribute the strong spectral shifts ($\delta\lambda/\delta n$) to the long resonant wavelengths which are just below the water absorption band at 1900 nm and the reduced substrate effect introduced by the etching of the glass substrate.³¹ This is further corroborated by simulations comparing the situation with and without additional glass etch, showing a 30% increase in peak shift sensitivity for the subradiant BDD and 45% for the BQD Fano mode upon etching. Figure S3 in the Supporting Information shows electric field intensity $|E|^2$ profiles further illustrating the effect of substrate etching on the available sensing volume. The big advantage of the line shape engineered plasmon modes is manifested in the FoM sensitivity. The reduced line width of the subradiant BDD and BQD Fano modes discussed above is directly reflected in an increased FoM with respect to the D_I and D_X modes. A FoM increase by more than 50% is obtained for both the BDD_{XI} and BQD_{XI} modes of the XI cavity with the smallest gap. Note that, although the main message here is the enhanced FoM sensitivity by radiative loss elimination, the bar and cross still outperform many other LSPR nanoparticles.^{1,47} For clinical applications it is more relevant to look at the spectral shift induced by target molecules bound either directly to the particle's Au surface or to a monolayer of receptor molecules preabsorbed on the metal (the surface-confined antigen). As the electromagnetic field of the LSPR is strongly confined to the particle surface on a scale of a few tens of nanometers, typically for small molecules near the metal surface the bulk sensitivity is a good indicator for the local sensitivity.^{29,49} Additionally, the cavity geometry can easily be rescaled to have resonances in the biological tissue penetration window (700–1000 nm) which would be necessary when working in a biological environment or to match typical Raman laser lines in the visible and NIR for SERS applications which can take advantage of the high field enhancements at the reduced radiative loss resonances.

In conclusion, we demonstrated high sensitivity LSPR RI nanosensors in the NIR. High spectral shifts were obtained by spectrally tuning the resonances as far as possible in the NIR while retaining a strong optical signal in experiments with microfluidic devices in aqueous environment and by applying a dry plasma etch of the substrate supporting the planar sensors, both leading to a dramatic increase in available sensing volume. A nanocross geometry was introduced as a new building block for coherently coupled LSPR nanocavities. It was shown experimentally, and supported by simulations, that coherent near-field coupling of the broad dipole and sharp quadrupole modes in the cross to the dipole resonance in a bar resulted in subradiant and Fano resonances in an XI arrangement with strongly reduced line widths. These cavities were used to present for the first time a detailed experimental analysis and comparison of the bulk RI sensitivity of radiative damping engineered coherent plasmonic nanocavities. The spectral narrowing realized in the subradiant and Fano resonances led to the highest FoM reported to date for individual nanoparticle type LSPR sensors without the need for sensitive single particle measurements. A full spectrum fit based on an analytical Fano model was put forward as a robust and reliable method for consistent spectral analysis of the complex asymmetric LSPR spectra. Refractive index sensitivities exceeding 1000 nm/RIU with a FoM reaching 5 in the NIR were obtained. By further fine-tuning of the geometrical parameters an even further increase in sensing performance and quality factors is expected, making these nanocross systems valuable platforms for biochemical sensing applications as well as plasmonic lasing. The use of a microfluidic chip device suggests easy integration of this type of LSPR sensor in lab-on-chip environments with low chemical consumptions.

■ ASSOCIATED CONTENT

S Supporting Information. Description of LSPR modes in XI structure and extended versions of Tables 1 and 2. This material is available free of charge via the Internet at <http://pubs.acs.org>.

AUTHOR INFORMATION

Corresponding Author

*Electronic address: niels.verellen@fys.kuleuven.be.

ACKNOWLEDGMENT

N.V. acknowledges support from the Methusalem funding by the Flemish Government. P.V.D. acknowledges financial support from the F.W.O. (Flanders). K.L. acknowledges financial support from the IWT (Flanders). We thank Jos Moonens for e-beam assistance.

REFERENCES

- (1) Liao, H.; Nehl, C. L.; Hafner, J. H. *Nanomedicine* **2006**, *1*, 201–208.
- (2) Maier, S. A. *Plasmonics: Fundamentals And Applications*; Springer-Verlag: New York, 2007.
- (3) Anker, J. N.; Hall, W. P.; Lyandres, O.; Shah, N. C.; Zhao, J.; Duyne, R. P. V. *Nat. Mater.* **2008**, *7*, 442–453.
- (4) Prodan, E.; Radloff, C.; Halas, N. J.; Nordlander, P. *Science* **2003**, *302*, 419–422.
- (5) Wang, H.; Wu, Y.; Lassiter, B.; Nehl, C. L.; Hafner, J. H.; Nordlander, P.; Halas, N. J. *Proc. Natl. Acad. Sci. U.S.A.* **2006**, *103*, 10856–10860.
- (6) Davis, T. J.; Gómez, D. E.; Vernon, K. C. *Nano Lett.* **2010**, *10*, 2618–2625.
- (7) Mukherjee, S.; Sobhani, H.; Lassiter, J. B.; Bardhan, R.; Nordlander, P.; Halas, N. J. *Nano Lett.* **2010**, *10*, 2694–2701.
- (8) Fan, J. A.; Wu, C.; Bao, K.; Bao, J.; Bardhan, R.; Halas, N. J.; Manoharan, V. N.; Nordlander, P.; Shvets, G.; Capasso, F. *Science* **2010**, *328*, 1135–1138.
- (9) Brown, L. V.; Sobhani, H.; Lassiter, J. B.; Nordlander, P.; Halas, N. J. *ACS Nano* **2010**, *4*, 819–832.
- (10) Aydin, K.; Pryce, I. M.; Atwater, H. A. *Opt. Express* **2010**, *18*, 13407–13417.
- (11) Neubrech, F.; García-Etxarri, A.; Weber, D.; Bochterle, J.; Shen, H.; Lamy de la Chapelle, M.; Bryant, G. W.; Aizpurua, J.; Pucci, A. *Appl. Phys. Lett.* **2010**, *96*, No. 213111.
- (12) Christ, A.; Ekinici, Y.; Solak, H. H.; Gippius, N. A.; Tikhodeev, S. G.; Martin, O. J. F. *Phys. Rev. B* **2007**, *76*, No. 201405.
- (13) Christ, A.; Martin, O. J. F.; Ekinici, Y.; Gippius, N. A.; Tikhodeev, S. G. *Nano Lett.* **2008**, *8*, 2171–2175.
- (14) Bachelier, G.; Russier-Antoine, I.; Benichou, E.; Jonin, C.; Fatti, N. D.; Vallée, F.; Brevet, P.-F. *Phys. Rev. Lett.* **2008**, *101*, No. 197401.
- (15) Fedotov, V. A.; Rose, M.; Prosvirnin, S. L.; Papasimakis, N.; Zheludev, N. I. *Phys. Rev. Lett.* **2007**, *99*, No. 147401.
- (16) Zhang, S.; Genov, D. A.; Wang, Y.; Liu, M.; Zhang, X. *Phys. Rev. Lett.* **2008**, *101*, No. 047401.
- (17) Sonnefraud, Y.; Verellen, N.; Sobhani, H.; Vandenbosch, G. A.; Moshchalkov, V. V.; Van Dorpe, P.; Nordlander, P.; Maier, S. A. *ACS Nano* **2010**, *4*, 1664–1670.
- (18) Verellen, N.; Sonnefraud, Y.; Sobhani, H.; Hao, F.; Moshchalkov, V. V.; Van Dorpe, P.; Nordlander, P.; Maier, S. A. *Nano Lett.* **2009**, *9*, 1663–1667.
- (19) Luk'yanchuk, B.; Zheludev, N. I.; Maier, S. A.; Halas, N. J.; Nordlander, P.; Giessen, H.; Chong, C. T. *Nat. Mater.* **2010**, *9*, 707–715.
- (20) Liu, N.; Langguth, L.; Weiss, T.; Kastel, J.; Fleischhauer, M.; Pfau, T.; Giessen, H. *Nat. Mater.* **2009**, *8*, 758–762.
- (21) Neubrech, F.; Pucci, A.; Cornelius, T. W.; Karim, S.; García-Etxarri, A.; Aizpurua, J. *Phys. Rev. Lett.* **2008**, *101*, No. 157403.
- (22) Hao, F.; Nordlander, P.; Sonnefraud, Y.; Van Dorpe, P.; Maier, S. A. *ACS Nano* **2009**, *3*, 643–652.
- (23) Mirin, N. A.; Bao, K.; Nordlander, P. J. *Phys. Chem. A* **2009**, *113*, 4028–4034.
- (24) Liu, N.; Weiss, T.; Mesch, M.; Langguth, L.; Eigenthaler, U.; Hirscher, M.; Sönnichsen, C.; Giessen, H. *Nano Lett.* **2010**, *10*, 1103–1107.
- (25) Lassiter, J. B.; Sobhani, H.; Fan, J. A.; Kundu, J.; Capasso, F.; Nordlander, P.; Halas, N. J. *Nano Lett.* **2010**, *10*, 3184–3189.
- (26) Bergman, D. J.; Stockman, M. I. *Phys. Rev. Lett.* **2003**, *90*, No. 027402.
- (27) Zheludev, N. I.; Prosvirnin, S. L.; Papasimakis, N.; Fedotov, V. A. *Nat. Photonics* **2008**, *2*, 351–354.
- (28) Zhao, J.; Zhang, X.; Yonzon, C. R.; Haes, A. J.; Van Duyne, R. P. *Nanomedicine* **2006**, *1*, 219–228.
- (29) Yonzon, C. R.; Jeoung, E.; Zou, S.; Schatz, G. C.; Mrksich, M.; Van Duyne, R. P. *J. Am. Chem. Soc.* **2004**, *126*, 12669–12676.
- (30) Svedendahl, M.; Chen, S.; Dmitriev, A.; Käll, M. *Nano Lett.* **2009**, *9*, 4428–4433.
- (31) Dmitriev, A.; Håggglund, C.; Chen, S.; Fredriksson, H.; Pakizeh, T.; Käll, M.; Sutherland, D. S. *Nano Lett.* **2008**, *8*, 3893–3898.
- (32) Miller, M. M.; Lazarides, A. A. *J. Phys. Chem. B* **2005**, *109*, 21556–21565.
- (33) Wang, F.; Shen, Y. R. *Phys. Rev. Lett.* **2006**, *97*, No. 206806.
- (34) Chou, S. Y.; Krauss, P. R.; Renstrom, P. J. *Science* **1996**, *272*, 85–87.
- (35) Aksu, S.; Yanik, A. A.; Adato, R.; Artar, A.; Huang, M.; Altug, H. *Nano Lett.* **2010**, 2511–2518.
- (36) Williams, K.; Gupta, K.; Wasilik, M. J. *Microelectromech. Syst.* **2003**, *12*, 761–778.
- (37) Lumerical <http://www.lumerical.com>.
- (38) Johnson, P. B.; Christy, R. W. *Phys. Rev. B* **1972**, *6*, 4370–4379.
- (39) Liu, N.; Kaiser, S.; Giessen, H. *Adv. Mater.* **2008**, *20*, 4521–4525.
- (40) Chen, K.-P.; Drachev, V. P.; Borneman, J. D.; Kildishev, A. V.; Shalaev, V. M. *Nano Lett.* **2010**, *10*, 916–922.
- (41) Hao, F.; Sonnefraud, Y.; Van Dorpe, P.; Maier, S. A.; Halas, N. J.; Nordlander, P. *Nano Lett.* **2008**, *8*, 3983–3988.
- (42) Hao, F.; Nordlander, P.; Burnett, M. T.; Maier, S. A. *Phys. Rev. B* **2007**, *76*, No. 245417.
- (43) Ropers, C.; Park, D. J.; Stibenz, G.; Steinmeyer, G.; Kim, J.; Kim, D. S.; Lienau, C. *Phys. Rev. Lett.* **2005**, *94*, No. 113901.
- (44) Meier, M.; Wokaun, A. *Opt. Lett.* **1983**, *8*, 581–583.
- (45) Huang, C.; Bonroy, K.; Reekmans, G.; Laureyn, W.; Verhaegen, K.; De Vlaminck, I. D.; Lagae, L.; Borghs, G. *Biomed. Microdevices* **2009**, *11*, 1572–1581.
- (46) Sherry, L. J.; Chang, S.-H.; Schatz, G. C.; Duyne, R. P. V.; Wiley, B. J.; Xia, Y. *Nano Lett.* **2005**, *5*, 2034–2038.
- (47) Chen, H.; Kou, X.; Yang, Z.; Ni, W.; Wang, J. *Langmuir* **2008**, *24*, 5233–5237.
- (48) Nehl, C. L.; Liao, H.; Hafner, J. H. *Nano Lett.* **2006**, *6*, 683–688.
- (49) Murray, W. A.; Auguié, B.; Barnes, W. L. *J. Phys. Chem. C* **2009**, *113*, 5120–5125.